

Predicting Osteoarthritis Progression in Radiographs via Unsupervised Representation Learning

Tianyu Han^{1,*}, Jakob Nikolas Kather^{2,3,4}, Federico Pedersoli⁵, Markus Zimmermann⁵, Sebastian Keil⁵, Maximilian Schulze-Hagen⁵, Marc Terwoelbeck⁵, Peter Isfort⁵, Christoph Haarburger⁶, Fabian Kiessling^{7,8,9}, Volkmar Schulz^{1,7,8}, Christiane Kuhl⁵, Sven Nebelung⁵[†], and Daniel Truhn^{5,*}[†]

¹Physics of Molecular Imaging Systems, Experimental Molecular Imaging, RWTH Aachen University, Germany

²Department of Medicine III, University Hospital RWTH Aachen, Aachen, Germany

³Pathology and Data Analytics, Leeds Institute of Medical Research at St James's, University of Leeds, Leeds, UK

⁴Medical Oncology, National Center for Tumor Diseases, University Hospital Heidelberg, Heidelberg, Germany

⁵Department of Diagnostic and Interventional Radiology, University Hospital Aachen, Germany

⁶CheckupPoint GmbH, Munich, Germany

⁷Comprehensive Diagnostic Center Aachen (CDCA), University Hospital RWTH Aachen, Aachen, Germany

⁸Fraunhofer Institute for Digital Medicine MEVIS, Bremen, Germany

⁹The Institute for Experimental Molecular Imaging, RWTH Aachen University, Germany

[†]Both authors contribute equally

*Correspondence should be addressed to D.T (dtruhn@ukaachen.de) and T.H (tianyu.han@pmi.rwth-aachen.de)

Abstract

Osteoarthritis (OA) is the most common joint disorder affecting substantial proportions of the global population, primarily the elderly. Despite its individual and socioeconomic burden, the onset and progression of OA can still not be reliably predicted. Aiming to fill this diagnostic gap, we introduce an unsupervised learning scheme based on generative models to predict the future development of OA based on knee joint radiographs. Using longitudinal data from osteoarthritis studies, we explore the latent temporal trajectory to predict a patient's future radiographs up to the eight-year follow-up visit. Our model predicts the risk of progression towards OA and surpasses its supervised counterpart whose input was provided by seven experienced radiologists. With the support of the model, sensitivity, specificity, positive predictive value, and negative predictive value increased significantly from 42.1% to 51.6%, from 72.3% to 88.6%, from 28.4% to 57.6%, and from 83.9% to 88.4%, respectively, while without such support, radiologists performed only slightly better than random guessing. Our predictive model improves predictions on OA onset and progression, despite requiring no human annotation in the training phase.

Introduction

OA is the most common joint disorder affecting 10% of men and 18% of women over 60 years of age [1]. It is one of the most frequent causes of pain, loss of function, and disability in adults. In developed countries, the resulting socio-economic burden is high with cost estimates ranging between 1.0% and 2.5% of gross domestic products [2]. Despite its public impact, the understanding of its pathogenesis is limited: OA remains an enigmatic condition and so far treatment mainly consists of pain management with joint replacement for end-stage disease [3]. If patients that are likely to experience future onset or progression of OA are identified in a timely manner, they can be treated accordingly, either surgically or non-surgically, to at least halt disease progression. Moreover, early disease stages may be susceptible to new therapeutic approaches [4,5]. However, with current standard clinical tools differentiation remains difficult between patients who require preventive measures - that is those with a high probability of progression - and those who do not have to be treated.

Artificial intelligence (AI) will have a profound impact on medicine in the next decades. A special class of neural networks, generative adversarial network (GANs) as first introduced by Goodfellow et al. [6], is successfully applied in various medical tasks, e.g., medical image synthesis [7–9], cross-modality translation [10, 11], and anonymous data sharing [7]. In this work, we predict the future progression towards OA as an exemplary representative use of our method. We utilize GANs to explore the latent temporal trajectories of patients whose longitudinal knee joint radiographs (obtained at recurring visits) were used to infer model-based prognostication of OA onset and progression. Once the model is fully trained, the model-based prognostication relies exclusively on a patient’s baseline radiograph.

The rationale for our investigation is as follows: There are vast amounts of longitudinally acquired medical image data because of patient follow-up studies that contain follow-up examinations or because of screening examinations that contain valuable implicit image information about the onset or progression of a particular disease. However, this information is so far unusable for conventional machine learning models as the majority of data is unlabeled in the sense that no human-generated, machine-readable data is available. A direct mapping of the time course of the images in pixel space is futile due to the challenges associated with high dimensionality [12]. However, if the relevant image information can be represented in a low-dimensional space, their trajectory in this space over time can be mapped. From this, a vector field mapping the image appearance of changes with time can be generated from a sufficient number of longitudinally acquired image data and the time course of new samples can be estimated based on where in that space the first image is located and where the vector field at that position is pointing to. If operational, such a modeling-based approach may provide reliable predictions of disease onset and progression.

Results

The System Overview

We focus on generating a synthetic image that best represents how an existing radiograph of the knee will look like in the future. To realize this, we train a GAN - the improved StyleGAN [13] - to generate future representations of the knee radiographs. The training of the GAN can be performed with the images only, i.e., without the need of any labeling. Instead of modeling the probability density directly, a GAN model learns a projection from a simple latent distribution p_w to the complicated real data distribution p_g [14]. In practice, such a projection is parameterized by a deterministic feed-forward neural network, i.e., a generator G . We make use of the fact that a GAN that yields high-quality data must incorporate a high-level understanding of the semantics of the real data distribution p_r and by proxy of the structure of the latent space. This allows us to explore the signature of future onset or progression to OA. As shown in Fig. 1 a, we map existing knee radiographs to the learned manifold, i.e., we invert the generator $G^{-1}(x)$ that finds the latent vector w that best describes the image x . We then make use of the fact that every radiological image is accompanied by a time-stamp of its acquisition [15]. This allows us to construct the latent vector field, i.e., $G^{-1}(x_{\text{baseline}}) \rightarrow G^{-1}(x_{\text{follow-up}})$, that maps radiographs to their future state. We proceed as follows when predicting the future - yet unknown - radiograph that corresponds to an existing radiograph (Fig. 1b): We locate the nearest neighbor of the existing radiograph by computing and sorting the normalized cosine distance (equation 4) between latent vectors of the target x and all other knees y within the dataset. After having identified the m surrounding neighbors within the latent space (Fig. 2b), the predicted knee image can be generated by feeding the latent vector $G^{-1}(x) + \Delta w_x$ to the trained StyleGAN G , where Δw_x is computed based on the empirical progression of the latent vector of the neighboring knees (equation 5).

Prediction of Onset and Progression of OA

The proposed system generates a prediction of the most probable future radiograph based on its baseline. OA usually develops over years or even decades. We tested our approach over a time span of eight years on 1,290 patients from the Osteoarthritis Initiative (OAI) dataset [16] that had not been seen by the model before. Exemplary real baseline radiographs, their real follow-up radiographs (obtained at the eight year follow-up visit), and their corresponding synthesized counterparts (generated based only on the real baseline) are shown in Fig. 2c and d. For patients exhibiting OA progression (Fig. 2c), the generated synthesized images demonstrate classic signs of OA, most notably joint space narrowing (as indicated by the red arrows), which is not present in non-progressing knee joints (Fig. 2d).

The task of estimating progression risks solely based on features provided by the baseline radiographs is challenging, even for experienced radiologists (Fig. 1c). To compare what is achievable with supervised

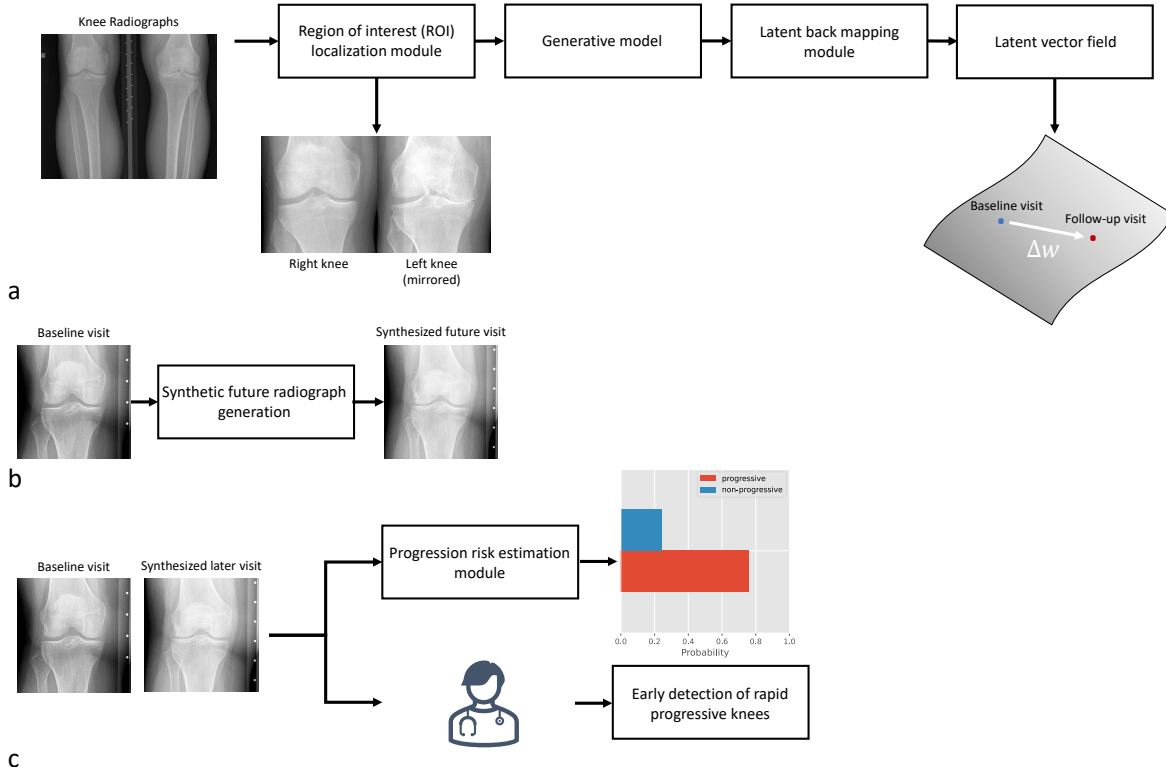


Fig. 1. Schematic Overview of Model-Based OA Predictions on Radiographs. (a) On the original knee radiographs (bilateral, posteroanterior projections, and fixed flexion), the image region containing the knee joints is identified. Images are cropped accordingly, and a generative model is trained to generate synthetic radiographs from a vector in a low-dimensional latent space. Corresponding original images are then back mapped to the point in latent space best matching the synthetic image (equation 5). Pairs of images of the same patient but at different time points are used to generate a vector field in latent space. (b) A knee radiograph with unknown future OA onset and progression can be mapped to its latent nearest neighbor at a follow-up visit using the vector field. (c) The progression risk is assessed by the trained model or by clinical radiologists.

learning based on the existing dataset, we finetuned a ResNet-50 classifier pre-trained on ImageNet dataset [17] that tries to identify progressors based on baseline radiographs in a supervised end-to-end manner. We found that the classifier is no better than random guessing in predicting OA onset or progression, i.e., the area under the receiver operating characteristic curve (ROC-AUC) was 0.52. However, our generative model achieved a substantially higher ROC-AUC of 0.69 on the OAI test set (Fig. 3a). A more detailed summary of performance metrics and confidence intervals (CI) can be found in Supplementary Table S3. To test if our algorithm generalizes well on external data, we evaluated the predictive model’s performance (as trained using the OAI data) on the independent Multi-center Osteoarthritis Study (MOST, $n=3,015$ participants), label distribution listed in Table S1) using our method in Fig. S7. As shown in Table S4 and in consistency with the data on the OAI dataset, our method achieves a significantly higher ROC-AUC of 0.64 (p -value < 0.001 , determined using bootstrapping) than its supervised counterpart with a ROC-AUC of 0.54.

Predicting the future state of a progressive disease via the latent nearest neighbor algorithm relies on two hyperparameters: the size of data that can be embedded into latent space, and the number of nearest neighbors considered (5). To verify that larger datasets are necessary for accurate predictions, we randomly subsampled the OAI training set to 1% (443 radiographs), 10% (4,433 radiographs), and 50% (22,163 radiographs). Fig. 4a demonstrates that incorporating more data points into the latent space improves the performance (in terms of ROC-AUC) of the proposed method. Related metrics and confidence intervals (CI) can be found in Supplementary Table S5. We evaluated the stability of our method with respect to the hyper-parameter m that denotes the number of nearest neighbors taken into account in the generation of future synthetic radiographs. As demonstrated in Fig. 4b and Table S6, only a minor performance change is observed when averaging multiple vectors of the nearest neighbors in the latent space.

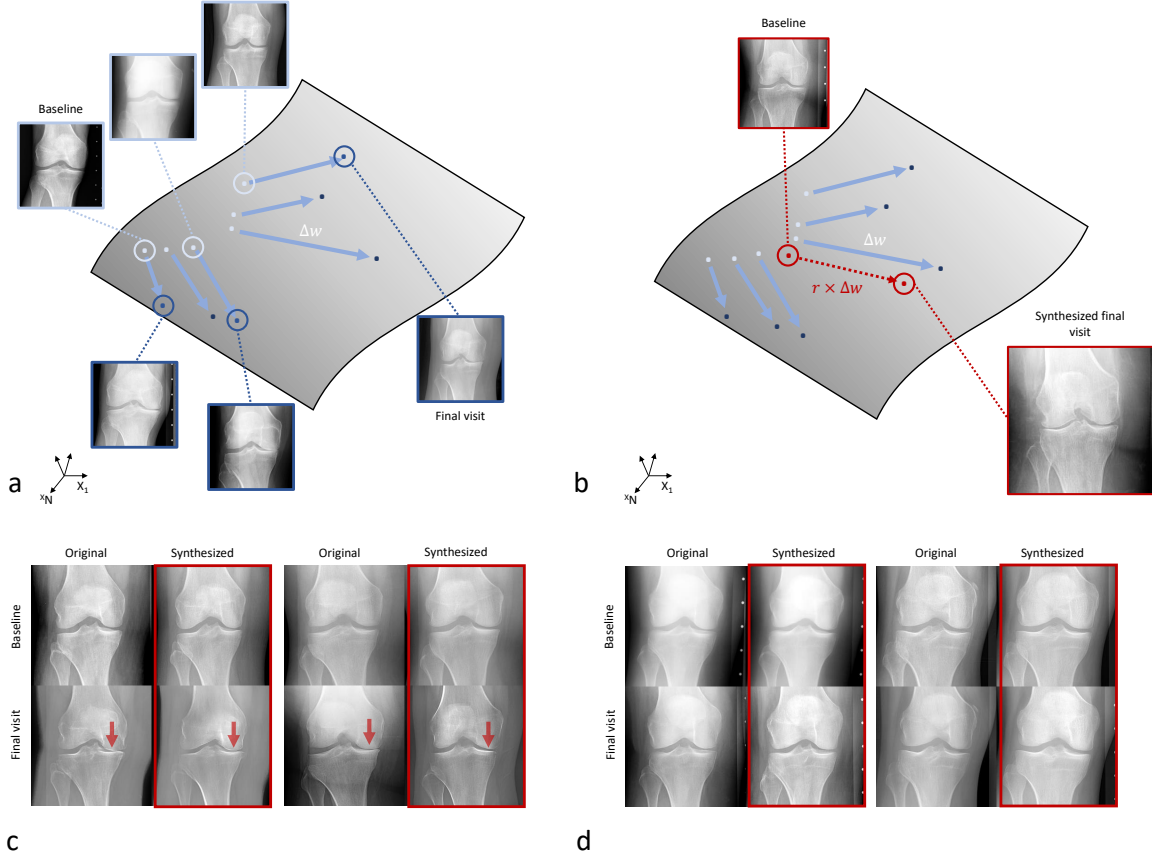


Fig. 2. Visualization of the Latent Nearest-neighbor Approach. (a) Through back mapping, knee radiographs (with a resolution of 256×256) are mapped to 512-dimensional vectors in the latent space. OA onset or progression is derived by computing the vector Δw that connects the baseline (white dots) to the follow-up radiograph (dark dots) of each patient. The latent space is populated by the longitudinal image data from OAI. (b) Visual explanation of the predicted follow-up radiographs. When predicting the future image morphology of a baseline knee radiograph x , x is firstly mapped to the 512-dimensional latent space ($G^{-1}(x)$). Its nearest neighbors are identified by calculating normalized cosine distances (equation 4), and the vector mapping the baseline to the follow-up image is determined via equation 5. The future appearance of the knee is then generated by feeding $G^{-1}(x) + \Delta w_x^{nn}$ to the StyleGAN G . (c), (d) Model predictions on knee joints that demonstrate OA progression (c) and that remain stable (d). Each knee joint is visualized in a 2×2 grid where the ground truth and the model predicted outcome are shown in the lower left and lower right panel, respectively. As a sign of progressive OA, joint space narrowing and subchondral opacification are indicated by the red arrows in (c). Note that the increasing severity of these OA features is correctly predicted by the model.

Model Assisted Identification of OA Onset and Progression By Humans in the Loop

Table 1: Mean Ratings of Radiologists in Detecting OA Progressive Knees

Model support	Sensitivity (95% CI)	Specificity (95% CI)	PPV (95% CI)	NPV (95% CI)	Fleiss' kappa
no	0.421 (0.275, 0.567)	0.723 (0.592, 0.853)	0.284 (0.244, 0.324)	0.839 (0.822, 0.856)	0.278
yes	0.516 (0.413, 0.618)	0.886 (0.791, 0.981)	0.576 (0.460, 0.692)	0.884 (0.870, 0.898)	0.484

In total, 486 knee radiographs were rated by seven radiologists for detecting rapid progressive knees (95 out of 486). This reader test consists of two phases: identification of progressors based on baseline radiographs or combining baseline radiograph information together with our model assisted prediction. Fleiss' kappa was computed to represent the inter-reader agreement. Abbreviations: PPV: positive predictive value, NPV: negative predictive value.

Assessing future OA onset or progression based on radiographs is challenging and therefore not routinely

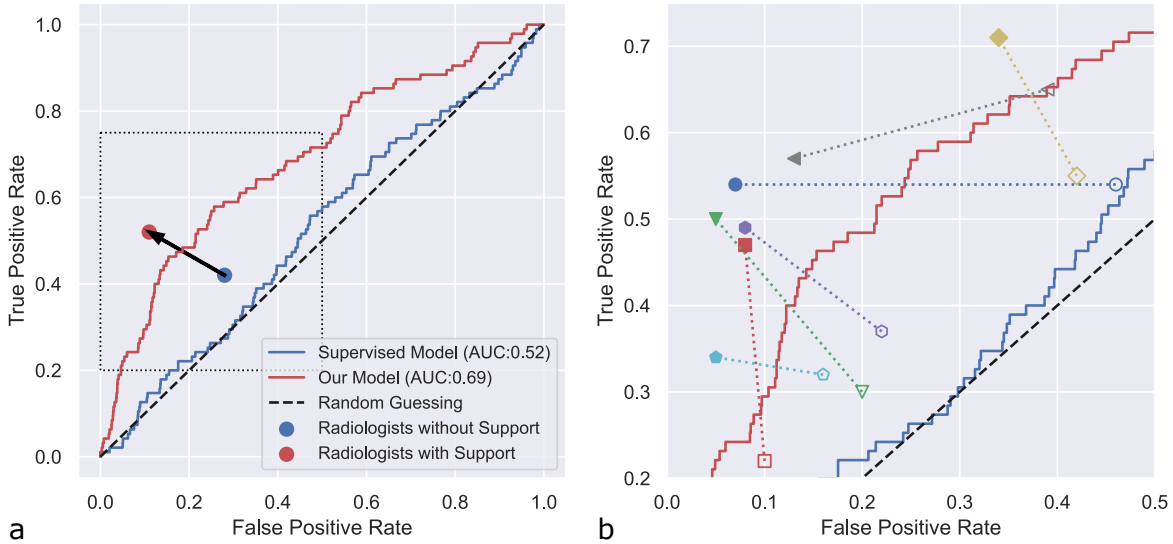


Fig. 3. Classification Performance of the Supervised and Unsupervised Models in Determining OA Progression. (a) ROC curves of the supervised classification network (blue) and our unsupervised approach (red). The proposed method outperforms the supervised model in terms of ROC-AUC (p -value < 0.001). The average performance of all radiologists without and with the support by the model is plotted as a blue and red dot, individually. Both sensitivity and specificity are increased when support by the model is provided (black arrow). (b) Zoomed-in region of the dotted rectangular area of the ROC (as outlined in a) with individual radiologists represented by open shapes (without model support) and filled shapes (with model support).

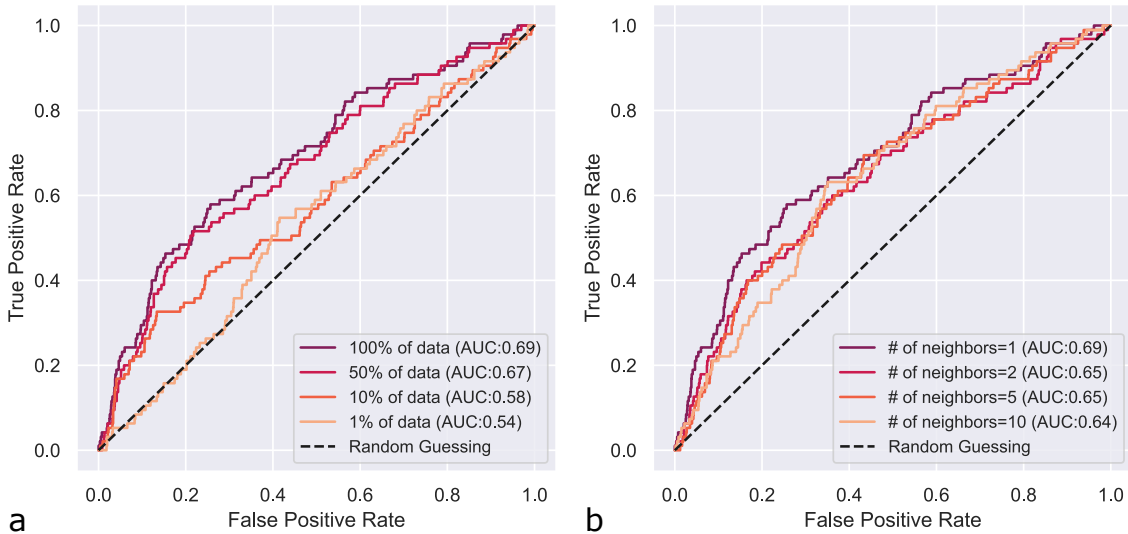


Fig. 4. System Performance as a Function of Training Data Size and the Number of Nearest Neighbors. (a) ROC curves with respect to different amounts of training data from the OAI. ROC-AUC was improved by including more data points into the image manifold. (b) Classification performance with respect to variable numbers of nearest neighbors that are utilized to determine the onset or progression of OA. Classification AUC when utilizing 1, 2, 5, or 10 nearest neighbors was comparable (see p -value in Table S6), indicating that adjacent samples in the latent space encode similar information.

performed by radiologists. Radiologists are rather trained to assess the radiograph at the time of presentation. We hypothesize that radiologists who are provided with the predicted future radiograph of a patient can better assess the onset or progression of OA.

After defining "OA progression" as developing more and/or severe radiographic signs of OA or developing any radiographic signs of OA where there were none before, we assigned radiologists to two experiments in random order: A) to predict whether the patient will have OA progression based on the present radiograph only B) to predict whether the patient will have OA progression based on the present radiograph and the

synthesized future radiograph generated by our model. In total, seven experienced clinical radiologists (with 4, 7, 6, 8, 17, 8, and 8 years of experience in musculoskeletal radiology) were asked to participate in both experiments. In experiment A, most radiologists were not able to reliably differentiate between the two groups, except for the radiologist with 17 years of experience, see Fig. 3 and Fig. S6. We found that the performance among radiologists varied significantly: sensitivity ranged from 22% to 65% and specificity ranged from 54% to 90% (see Fig. 3b and Table S2). This is not surprising given the fact that radiologists have very limited experience with predicting the course of OA over many years. In test B, results were substantially improved by the additional informative presentation of the synthesized future radiograph. As shown in Fig. 3b and Table S2, both sensitivity and specificity consistently improved to ranges of 34% to 71% and 66% to 95% and all radiologists reached a significantly better performance as quantified by the ROC-AUC. Comparing these results to the fully automated assessment with our unsupervised model, we find that our algorithm outperforms almost all radiologists in test A: only the most senior radiologist is on par with the unsupervised model. If supported by the model, radiologists -both individually and overall- consistently outperform the model (Test B, Fig. 3), which highlights the fact that human and artificial intelligence are complementary. It is also noteworthy, that AI-support helps the radiologists to rate the radiographs more consistently: while Fleiss' kappa is 0.278 for test A, the agreement between radiologists is higher in test B with a kappa of 0.484, see Table 1.

Visualization of OA Progression

Our test with human experts suggests that future states of disease as predicted by the proposed generative model are beneficial to clinicians and can aid in prognostication. Moreover, the model seems to be capable of predicting the image appearance of a knee radiograph several years into the future. To visualize the future OA onset or progression we generate synthesized radiographs at 1, 2, 4, 6, and 8 years into the future (based solely on the baseline radiograph) for all patients who returned for follow-up visits in these intervals, i.e., for whom the real counterparts are available. We find that the GAN smoothly interpolates the image appearance of progression from healthy to osteoarthritic knees and is in agreement with the changes observed in the real radiographs, see Figure 5. We then calculate the progression score both for the real and the synthesized radiographs and plot their respective time courses in Fig. 5. Again we find, that the two curves correctly demonstrate OA onset or progression, even though changes in the real radiograph seem to be preceded by changes in the synthesized radiograph. It is also interesting to note that the synthesized radiograph - in accordance with the real radiograph - visualizes an increase in soft tissues around the knee as a sign of weight gain, often a cause for OA onset or progression due to increased mechanical load.

Diagnostic Information is Preserved in the Latent Space

When representing a radiograph solely by a point in the latent space (i.e. 512-dimensional vector), diagnostic information might get lost. To test whether this is the case, we conducted additional experiments. Important diagnostic information contained in the images is the grading according to Kellgren-Lawrence-Score (KLS) and the knee injury and osteoarthritis outcome score (KOOS). We followed the approach given in [18, 19] and performed the classification task solely on latent vectors - i.e., not the images themselves were used for training, but their low-dimensional condensed representation in latent space. We trained the algorithm to extract the the KLS grade and the KOOS. Data was partitioned as before (see Fig S1) and the latent vector for a specific knee was calculated following Algorithm 1. For the classification tasks, we trained a shallow neural network with only one hidden layer on the latent vectors of the OAI training and validation sets. Results are given in Fig. S9. When evaluated on the test set, the KOOS classifier reached a state of the art AUC of 0.69 (95% CI: 0.651, 0.719), a sensitivity of 0.61 (95% CI: 0.56, 0.66), and a specificity of 0.66 (95% CI: 0.623, 0.696), on par with algorithms trained on the full images [20].

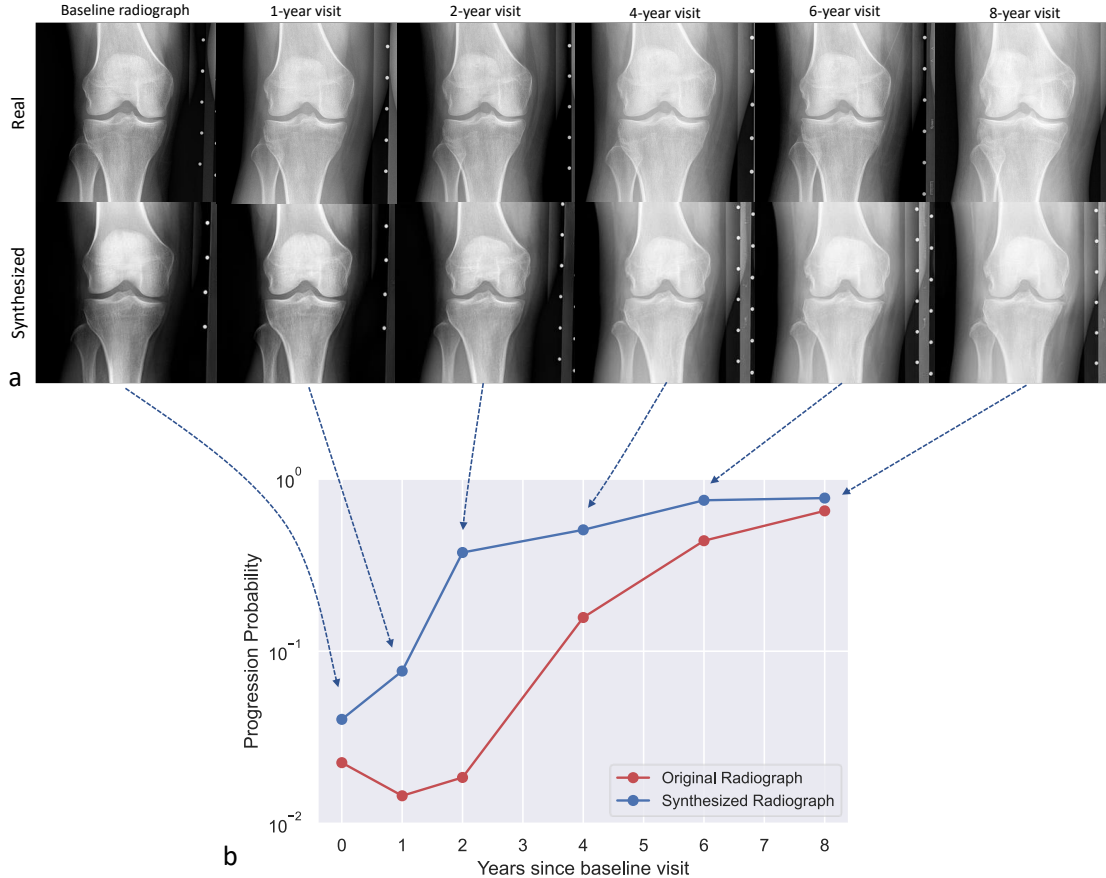


Fig. 5. Longitudinal Evolution of a Participant with OA Progression as Reflected by Original and Synthetic Radiographs. Temporal evolution of the left knee of an 61-year-old female participant from the OAI. This was read as displaying no signs of OA at baseline (KLS=0) and presented with mild OA (KLS=2) after 8 years. (a) Original radiographs (upper row) and corresponding model-based synthetic predictions (lower row) at baseline as well as at the 1-year, 2-year, 4-year, 6-year, and 8-year follow-up visits. Original and synthetic radiographs show similar intra-articular changes. Please also note the similar periarticular changes in terms of increased soft tissue around the joint. (b) Based on the images, the respective progression probability was computed for the synthetic (blue) and original radiographs (red). Both curves correctly arrive at a high probability of OA progression, while the synthesized radiographs seem to precede the changes as compared to the original radiographs.

Discussion

In this work, we demonstrated the diagnostic and the prognostic potential of using unlabeled data to train a machine learning algorithm. We focused on knee radiographs, in particular on OA onset and progression. The algorithm was tested on a multi-center and multi-trial dataset and we were able to show that the classification performance of radiologists can be improved by a wide margin. As OA prognostication remains challenging despite enormous clinical and scientific research efforts, the identification of patients who are susceptible to develop OA or to undergo OA progression is of paramount importance to guide treatment and to potentially facilitate new preventive or curative treatment strategies. Even though our predictive model has been validated on high-quality study collectives of the OAI and MOST trials and remains to be validated in less homogeneous clinical collectives, the systematic use of unlabeled data and unsupervised learning suggests a promising alternative path forward to improve OA prognostication based on predictive models. Importantly, the presented method can be applied to a plethora of general medical conditions in which the future progression of a disease is important for medical decision making. No dedicated labeling of data is needed, as the imaging devices produce a time-stamp on each acquired radiological image by default. Synthetic radiological images have been used before to alleviate the problems associated with data sharing [7] or to generate synthetic CT datasets from MRI datasets [21]. However, no study so far has involved synthetic radiological images and latent space trajectories into disease prognostication and, secondarily, clinical decision-making. Possible application scenarios

include the use of brain MRI to monitor and predict the onset or progression of Alzheimer’s disease or other neuro-degenerative disorders to act early and to prevent further progression [22]. Indeed, it has been shown that prediction of the progression in patients with Alzheimer’s disease based on variables extracted through deep neural networks might be a promising approach [23–25]. Similar needs arise in the progression of patients with liver fibrosis towards liver cirrhosis [26], the progression of osteoporosis [27], the course of cardiovascular diseases [28], or diabetes and its complications [29]. These application scenarios require big datasets and potential sharing of data across institutions and borders, but this is in reach given the national efforts to implement screening programs [30].

This study and the predictive model have limitations: First, to train the generative model a large amount of data is needed - for plain radiographs as used in this work, we utilized approximately 50,000 images. It can be expected that a higher number of samples will be needed for image data that contain higher dimensional information, e.g., three- or even four-dimensional time-resolved MRI or CT images. Second, in order for the model to make accurate predictions, a clear progression with corresponding image changes needs to be present. This is clearly the case for OA and probably for several other diseases that were mentioned above as potential application scenarios. Previous work has for example focused on predicting brain tumor size [31, 32]. While these models assumed a Gaussian distribution in latent space, allowing for convenient sampling, the unbounded latent in our work focusses on sample quality to facilitate a hybrid approach for clinical practice. Note, that our approach can be expanded to quantify uncertainty: we can progressively add more observations to the latent space and measure the information gain. Third, we found in Fig S8 that sometimes the system correctly predicts the progression of OA, yet bases its prediction on implausible image features. Here, the consistent implementation of the model’s output, e.g., by saliency maps, may improve explainability and comprehensibility on the part of the user. Fourth, the OAI and MOST datasets are well curated and provide standardized image quality due to stringently implemented acquisition and post-processing techniques. The predictive model’s successful application on these datasets does not necessarily translate to clinical applicability and benefit as radiographs acquired in clinical contexts may display larger variability in image quality. In conclusion, we introduce and validate a novel predictive model that uses unsupervised learning to provide information on OA onset and progression. Beyond OA, this proof-of-concept study highlights the potential of unsupervised learning schemes, generative models, and latent space trajectories to make substantiated predictions on future disease states in nearly all fields of medicine without necessitating any additional labels.

Methods

Development and Testing Datasets

The system was developed on data from the Osteoarthritis Initiative (OAI), consisting of a total number of 26,525 bilateral fixed flexion plain film radiographs from 4,796 participants with OA of the knee or at risk of developing knee OA [16]. In this longitudinal cohort study, the imaging, biochemical, and constitutional findings associated with knee OA have been investigated and documented from February 2004 to October 2015. Briefly, the right and the left knees of participants were imaged together on 14×17 inch films. In total, we utilized a pre-trained Hourglass network and extracted 52,981 (separated left and right) knee radiographs with a region of $140\text{mm} \times 140\text{mm}$ from all participants who were regularly imaged from baseline to the 96-month follow-up [33]. During the development of this study, the input knee images were flipped to the right knee configuration and resized to 256×256 by bilinear interpolation. Both quantitative and semi-quantitative assessments, such as the joint space width and the KLS, were available for most radiographs (43,132 knee radiographs from 3,944 patients) from the OAI. In this study, we used the KLS as a quantitative measure an image’s morphological changes reflective of OA onset or progression. As shown in Fig S1, participants were randomly allocated to training, validation, and hold-out test sets. The test set was kept separate during the development phase of the algorithm and was only used to test the algorithm’s performance after parameter tuning had been finished. Since the KLS is not needed in the unsupervised approach, the unlabeled radiographs could be used as well and were included in the model development loop (9,849 radiographs from 852 patients). Supplementary Table S1, describes demographic characteristics and the KLS for relevant subsets of the OAI dataset.

An independent dataset from the Multi-center Osteoarthritis Study (MOST) [34] was also used to validate the system’s performance and generalization in another dataset from another trial. Similar to the OAI dataset, the MOST dataset is a longitudinal, prospective study that recruited more than 3,026 participants for five follow-up visits at 15, 30, 60, 72 and 84 months. In the MOST dataset, all 19,340 knee radiographs labeled with KLS (bilateral, standing fixed-flexed posteroanterior views) were used solely for testing our proposed predictive model. Detailed label statistics for the MOST datasets can be found in table S1. Ethical approval for collecting all subject information was provided by the OAI and MOST.

Details of System Modules

In general, our system is trained to take the baseline knee radiograph and automatically produce the future knee morphology as well as the risk score predicting whether the patient will suffer from OA onset or progression in the next years. The proposed modular approach consists of a generative StyleGAN, a latent back-mapping module, a synthetic future radiograph module, and a progression risk estimation module.

StyleGAN and Training Details

Our approach relies on training a generative model that learns high-level representations of input knee radiographs. A GAN consists of a generator network and a discriminator network. The generator network G projects a simple latent distribution P_z to a more complex data distribution P_g . Next, a feed forward neural network, i.e., a discriminator D , is used to directly measure the distributional distance between P_g and a real data distribution P_r . The training process of our GAN follows the original approach by solving the min-max problem $\min_G \max_D L(G, D)$ via training D and G alternately. The objective function of the GAN can be expressed as:

$$\begin{aligned} L_D &= \min_D \mathbb{E}_{x \sim P_r(x)} [-\log D(x)] + \mathbb{E}_{x \sim P_g(x)} [-\log(1 - D(x))] \\ L_G &= \min_G \mathbb{E}_{z \sim P_z(z)} [-\log D(G(z))]. \end{aligned} \tag{1}$$

Goodfellow et al. suggest this version of the G loss L_G in equation 1 to circumvent the saturation of G during the early phase of training. However, plenty of observations have been made on problems such as the instability of training a GAN to truly converge and the mode collapse issue in GAN-generated samples. It has been widely shown that optimizing the objective in equation 1 via simultaneous gradient descent does not guarantee the convergence towards the Nash equilibrium point [6]. Therefore, it’s necessary to add additional regularization strategies to stabilize the training. In this work, we regularize the training process of D θ_d via adding a gradient penalty term R_1 to L_D :

$$R_1(\theta_d) = \frac{\gamma}{2} \mathbb{E}_{x \sim p_r(x)} \|\nabla_x D \theta_d(x)\|^2. \tag{2}$$

We set the R_1 regularization weighting factor to $\gamma = 10$ throughout the training process. Similarly, we enforce the smoothness of the G function θ_g with respect to the intermediate latent w by using the path length regularization [13]:

$$R_{pl}(\theta_g) = \mathbb{E}_{w,y \sim \mathcal{N}(0,I)} (\|\nabla_w G(w)y\|_2 - a)^2, \quad (3)$$

where y is randomly distributed Gaussian noise with the same shape as the generated image $G(w)$ and the constant a is the running average of $\mathbb{E}_{w,y} \|\nabla_w G(w)y\|_2$. This G regularization is of particular importance to our method as it guarantees meaningful interpolations in the intermediate latent space and makes the G inversion easier [13]. Figure S3 a plots the output logits for both real and generated samples from D during training. Regularization on both D and G are also plotted in Figure S3 b.

To measure whether the generated images converged to realistic radiographs, we continuously measured the Fréchet Inception Distance (FID) between a set of 50,000 real and synthesized pairs during training [35]. We found that the FID decreased nearly monotonically, indicating that the general appearance of the generated images approaches that of real radiographs. The corresponding figures depicting the evolution of the FID are given in Fig. S3 c. However, a single FID score cannot make conclusions about the generation ability, i.e., precision and recall, of the trained GAN [36]. We additionally computed the distribution-wise precision and recall parameters to characterize our GAN and to pick the best performing model. As shown in Figure S3 d, we selected the best performing GAN model with the highest precision and recall (indicated by the red arrow). The description of the selected model characteristics to the target distribution of knee radiographs is depicted in a precision-recall curve [36] in Figure S3 e.

We employ the improved G architecture of StyleGAN [13]. Unlike conventional generators, Karras et al. design additional mapping layers f (two-layer perceptron) that non-linearly project the simple Gaussian latent z into an intermediate latent space W with the same 512 dimensions. It has been shown that feature disentanglement becomes achievable in the intermediate latent space W as it does not have to be bounded by any fixed, e.g., Gaussian or uniform, distribution for convenient sampling. In this study, we therefore refer to the latent vector as vectors w in W . To control feature appearance, as shown in Fig. S2 c-e, we pass the affine transformed latent vector w to the convolution layers of the StyleGAN G [13]. The G architecture resulted in a final spatial resolution of 256×256 is shown in Fig. S2. We picked the leaky rectified linear unit (LReLU) with a negative slope of 0.2 and weight demodulation [13] as the activation function and normalization in G layers. Similarly, in D, we chose LReLU and Sigmoid as activation functions for convolution layers and the final classifier layer separately. During training, we used two Adam optimizers [37] with the same learning rate of 0.0025 for both G and D, and the mini-batch size was set to 32 across two NVIDIA Titan RTX GPUs. Throughout the study, Pytorch v.1.8.1 was used for implementation [38].

Latent Back Mapping Module

Once the generative model is trained, a method is needed to map an existing knee radiograph x to a point w in latent space W such that the radiograph \hat{x} synthesized from w is a close representation of x . Technically, under the framework of StyleGAN, we need to optimize the intermediate latent vector w and noise maps n_i corresponding to different resolutions for reconstructing the counterpart of a target image x . To approximate the mapping function $G^{-1}(x)$, we compute the learned perceptual image patch similarity (LPIPS) [10], i.e., the Euclidean distance between embeddings of x and \hat{x} extracted by a pretrained VGG-16 network, as the cost function (Fig. S4 a). While optimizing n_i , we make sure no meaningful gradient from x is leaked to n_i during gradient descent by adding an auto-correlation regularization [13]. We additionally impose randomization to the latent w when evaluating the cost function in order to avoid trapping in a local minimum [39]. The cost was optimized by an Adam optimizer with an initial learning rate of 0.1. More details of the inverting a StyleGAN G are depicted in Algorithm 1. To test, whether the computed w is a good approximation of $G^{-1}(x)$, we computed the structural similarity index (SSIM) between 5,000 pairs of original and reconstructed radiograph of both the OAI and the MOST dataset in Fig. S4 b. As shown in Fig. S4 b, we observed that OAI reconstructed radiographs achieved SSIMs of around 0.8, while MOST reconstructed radiographs displayed slightly larger variability, most likely due to the fact that the GAN had been trained on OAI radiographs only. In addition, 500 random pairs of x and their corresponding $G(w)$ were also compared by one radiologist with 8 years of experience and checked visually for inconsistencies. In all 500 sample pairs, there was good agreement between the real and synthesized radiographs with no visually notable difference.

Algorithm 1 Inverting StyleGAN Generator $G^{-1}(x)$. We use default values of $\eta = 0.1$, $\alpha = 10^5$, and $n_z = 10,000$.

- 1: **Require:** A candidate baseline knee radiograph I ; a pretrained StyleGAN $G(w, n_i)$ with a mapping network $f(z)$; LPIPS loss function L_{LPIPS} ; noise regularization R ; learning rate schedule T .
 - 2: **Require:** a maximum learning rate η ; the number of latent code z sampled n_z ; the weight of noise regularization α ; a constant t scales the noise amplitude of w .
 - 3: **Output:** the optimized latent vector w that can reconstruct I .
 - 4:
 - 5: **for** $n = 1, \dots, n_z$ **do**
 - 6: Sample normally distributed latent code z_n
 - 7: Compute $\mu_w = \mathbb{E}_n f(z_n)$ and $\sigma_w^2 = \mathbb{E}_n \|f(z_n) - \mu_w\|_2^2$
 - 8: Initialize latent $w = \mu_w$ and noise map $n_i = \mathcal{N}(0, \mathbf{I})$
 - 9:
 - 10: **while** not converged **do**
 - 11: $w \leftarrow w + \mathcal{N}(0, 0.05\sigma_w t)$
 - 12: $L \leftarrow L_{\text{LPIPS}}(I, G(w, n_i)) + \alpha R(n_i)$
 - 13: $w \leftarrow w - \eta \nabla_w L$
 - 14: $n_i \leftarrow n_i - \eta \nabla_{n_i} L$
 - 15: $\eta \leftarrow T(\eta)$
 - 16: **return** w
-

Synthetic Future Radiograph Generation

In the first step, we construct a dictionary $D = \{w_i\}_{i=1}^N$ that contains mapped latent code w of OAI radiographs based on Algorithm 1. We conceptually construct a vector field \mathbf{V} that maps the points in the latent space W that belong to the baseline radiographs x^{baseline} to points in the latent space of the follow-up radiograph $x^{\text{follow-up}}$: $\mathbf{V} : G^{-1}(x^{\text{baseline}}) \rightarrow G^{-1}(x^{\text{follow-up}})$. Predicting the future state of a progressive knee x during inference is a combination of two steps: identification of the latent code w_x of the candidate’s knee (Algorithm 1), and modeling the future appearance of the knee radiograph via interpolating the latent vector field V . To interpolate the value of the vector field at new positions x , we employ the nearest neighbor interpolation with *nearest* defined via the normalized cosine distance

$$d(x, y) = \left\| \frac{w_x}{\|w_x\|_2} - \frac{w_y}{\|w_y\|_2} \right\|_2, \quad (4)$$

and the actual interpolation defined as:

$$\Delta w_x^{mn} = \frac{1}{m} \sum_{i=1}^m \frac{\Delta t^i}{\Delta T} \left[G^{-1}(x_i^{\text{follow-up}}) - G^{-1}(x_i^{\text{baseline}}) \right], \quad (5)$$

where m is the number of nearest neighbors, ΔT is the time interval denoting how far in the future the synthesized radiograph should be generated, and $G^{-1}(x_i)$ is the corresponding latent vector of the i -th nearest neighbor of x . The prediction of the future knee state can be obtained via feeding the mapped latent $w_{\hat{x}}$ and the computed vector difference Δw_x^{mn} to the generator, i.e., $G(w_x + \Delta w_x^{mn})$. This procedure was used to generate synthetic future radiographs for the human reader test.

Progression Risk Estimation Module

The risk prediction module takes in a baseline scan and its (synthesized) follow-up scan in the form of gray-scale knee radiographs to predict the OA progression risk. Previous studies solely utilized the baseline patient state, e.g., the radiological image or study, and tried to predict the future progression probability in an end-to-end fashion [40–42]. However, in this study, we can predict the morphological appearance of the radiograph at a future time point (Algorithm 2) and compute the risk based on the appearance of the synthetic radiograph as detailed above. Inside the module, we placed an adversarially trained ResNet-50 [43] that can correctly classify the KLS of the input knee radiograph. As indicated in Fig. S1, the classifier was developed and tested on 34,477 KLS-labeled knee radiographs from 2,654 participants and another 8,655 knee radiographs from 1,290 participants that were initially held out as the radiologists’ test set but were then included. The

Algorithm 2 Radiograph Prediction as Generated from the Latent Space

- 1: **Require:** A candidate baseline knee radiograph I ; a pretrained StyleGAN G ; the calculated mapping dictionary D of knees.
 - 2: **Require:** the number of nearest neighbors considered m .
 - 3: **Output:** Synthetic future radiograph of the candidate’s knee.
 - 4: get $w_I \leftarrow G^{-1}(I)$ from Algorithm 1
 - 5:
 - 6: **for** w_j in $D.keys()$ **do**
 - 7: $d(w_I, w_j) \leftarrow \left\| \frac{w_I}{\|w_I\|_2} - \frac{w_j}{\|w_j\|_2} \right\|_2$
 - 8: Sort w_j in $D.keys()$ according to distances $d(w_I, w_j)$
 - 9: Initialize $\Delta w_I^{nn} = 0$
 - 10:
 - 11: **for** w_i in set M containing latents for the m smallest distances $d(w_I, w_j)$ **do**
 - 12: $\Delta w_I^{nn} \leftarrow \frac{\Delta c_i}{\Delta T} (w_i^{follow-up} - w_i^{baseline}) + \Delta w_I^{nn}$
 - 13: **return** $I_{future} \leftarrow G(w_I + \frac{1}{m} \Delta w_I^{nn}, n_i = 0)$
-

ResNet classifier utilized the softmax loss function as its criterion. Additionally, to improve the interpretability of the classifier, we applied adversarial augmentation with an attack strength of $\epsilon = 0.005$ during the training process [43]. The classification performance of the ResNet, as well as its interpretable gradient saliency maps are shown in Fig. S5 a and b.

We denote x_i, x_j as baseline and follow-up knee radiographs respectively (Fig. 1c), and c_i, c_j as KLS classes for x_i and x_j ranging from 0 to 4. We defined patients with imminent OA onset and/or progression towards osteoarthritis changes as those, who showed progress of more than one KLS ($c_j - c_i > 1$) over scans. We then computed the probability of OA progression ($y = 1$) as a sum of joint probabilities $\{(c_i, c_j)\}$ which fulfill the condition that the KLS change is larger than 1, i.e., $c_j - c_i > 1$, between its prior and follow-up visit radiographs:

$$\begin{aligned} p(y = 1|x_i, x_j) &= \sum_{\{(c_j - c_i > 1)\}} p(\text{KLS} = c_i|x_i) \times p(\text{KLS} = c_j|x_j), \\ p(y = 0|x_i, x_j) &= 1 - p(y = 1|x_i, x_j). \end{aligned} \tag{6}$$

Clinical Reader Experiments

To identify patients who are in need of preventive care, it is important to differentiate between patient with imminent OA onset and/or progression towards osteoarthritic changes and patients with stable disease. We defined participants belonging to the group of progressors as those, who showed progress of more than one KLS over 8 years. We designed two different experiments: In experiment A, seven experienced radiologists were given only the baseline radiograph and were asked to predict whether a patient will experience the onset or progression of OA, or whether a patient exhibits a stable disease. In experiment B, the proposed generative model was used to synthesize the most probable imaging appearance (see section **Synthetic Future Radiograph Generation**) of the radiograph 8 years into the future based on the vector field in the latent space. The radiologists were then given the predicted synthesized radiograph next to the baseline radiograph as additional guiding help and were again asked to perform the same allocation into two groups. For both experiments, we randomly selected 468 participants and 486 knee radiographs (95 progression-positive as defined above) with a resolution of 256×256 out of the test set. All reading experiments were done on diagnostic computer monitors.

Statistical Analysis

For each of the experiments, we calculated the following parameters on the test set: ROC-AUC, sensitivity, and specificity. The cutoff value for deciding between the presence or non-presence of pathology was determined by minimizing $(1 - \text{sensitivity})^2 + (1 - \text{specificity})^2$ [44]. If not otherwise stated, standard deviations (SD) and 95% CI were extracted using bootstrapping with 10,000 redraws. The difference in metrics, such as ROC-AUC, sensitivity, and specificity, was defined as a Δ -metric. For the total number of $N = 1,000$ bootstrapping, models were built after randomly permuting predictions of two classifiers, and metric differences $\Delta - \text{metric}_i$ were

computed from their respective scores. We obtained the two-tailed p-value of individual metrics by counting all $\Delta - \text{metric}_i$ above the threshold Δ_{metric} . Statistical significance was defined as $P < 0.001$. For the clinical reader experiments, Cohen's kappa was used to calculate intra-reader agreement between experiments A and B for the same reader, while Fleiss' kappa was used to calculate inter-reader agreement between the seven radiologists.

Author contributions:

TH and DT devised the concept of the study, DT, SN, MS, MZ, FP, SK, and MH performed the reader tests. TH wrote the code and performed the performance studies. TH and DT did the statistical analysis. TH and DT wrote the first draft of the manuscript. All authors contributed to correcting the manuscript.

Disclosures of Conflicts of Interest:

JNK declares consulting services for Owkin, France and Panakeia, UK.

Funding sources

JNK is supported by the German Federal Ministry of Health (DEEP LIVER, ZMVI1-2520DAT111) and the Max-Eder-Programme of the German Cancer Aid (grant 70113864).

Data and materials availability:

All datasets used in this study are publicly available: the dataset of knee radiographs of the OAI and MOST datasets can be requested from <https://nda.nih.gov/oai/> and <https://agingresearchbiobank.nia.nih.gov/studies/most/>. The code used in this study is made fully publicly available under https://github.com/peterhan91/disease_progression.

References

- [1] S. Glyn-Jones, A. Palmer, R. Agricola, A. Price, T. Vincent, H. Weinans, and A. Carr, "Osteoarthritis," *The Lancet*, vol. 386, no. 9991, pp. 376–387, 2015.
- [2] M. Hilgsmann, C. Cooper, N. Arden, M. Boers, J. C. Branco, M. L. Brandi, O. Bruyere, F. Guillemin, M. C. Hochberg, D. J. Hunter, *et al.*, "Health economics in the field of osteoarthritis: an expert's consensus paper from the european society for clinical and economic aspects of osteoporosis and osteoarthritis (esceo)," in *Seminars in arthritis and rheumatism*, vol. 43, pp. 303–313, Elsevier, 2013.
- [3] J. W. Bijlsma, F. Berenbaum, and F. P. Lafeber, "Osteoarthritis: an update with relevance for clinical practice," *The Lancet*, vol. 377, no. 9783, pp. 2115–2126, 2011.
- [4] P. G. Conaghan, "Osteoarthritis in 2012: parallel evolution of oa phenotypes and therapies," *Nature Reviews Rheumatology*, vol. 9, no. 2, p. 68, 2013.
- [5] N. Arden and M. C. Nevitt, "Osteoarthritis: epidemiology," *Best practice & research Clinical rheumatology*, vol. 20, no. 1, pp. 3–25, 2006.
- [6] I. Goodfellow, J. Pouget-Abadie, M. Mirza, B. Xu, D. Warde-Farley, S. Ozair, A. Courville, and Y. Bengio, "Generative adversarial nets," *Advances in neural information processing systems*, vol. 27, 2014.
- [7] T. Han, S. Nebelung, C. Haarburger, N. Horst, S. Reinartz, D. Merhof, F. Kiessling, V. Schulz, and D. Truhn, "Breaking medical data sharing boundaries by using synthesized radiographs," *Science Advances*, vol. 6, no. 49, p. eabb7973, 2020.
- [8] V. Sandfort, K. Yan, P. J. Pickhardt, and R. M. Summers, "Data augmentation using generative adversarial networks (cycleGAN) to improve generalizability in ct segmentation tasks," *Scientific reports*, vol. 9, no. 1, pp. 1–9, 2019.
- [9] S. Kench and S. J. Cooper, "Generating three-dimensional structures from a two-dimensional slice with generative adversarial network-based dimensionality expansion," *Nature Machine Intelligence*, vol. 3, no. 4, pp. 299–305, 2021.

- [10] Z. Zhang, L. Yang, and Y. Zheng, “Translating and segmenting multimodal medical volumes with cycle- and shape-consistency generative adversarial network,” in *Proceedings of the IEEE conference on computer vision and pattern Recognition*, pp. 9242–9251, 2018.
- [11] C. Wang, G. Yang, G. Papanastasiou, S. A. Tsaftaris, D. E. Newby, C. Gray, G. Macnaught, and T. J. MacGillivray, “Dicyc: Gan-based deformation invariant cross-domain information fusion for medical image synthesis,” *Information Fusion*, vol. 67, pp. 147–160, 2021.
- [12] N. Altman and M. Krzywinski, “The curse (s) of dimensionality,” *Nat Methods*, vol. 15, no. 6, pp. 399–400, 2018.
- [13] T. Karras, S. Laine, M. Aittala, J. Hellsten, J. Lehtinen, and T. Aila, “Analyzing and improving the image quality of stylegan,” in *Proceedings of the IEEE/CVF Conference on Computer Vision and Pattern Recognition*, pp. 8110–8119, 2020.
- [14] J. Donahue, P. Krähenbühl, and T. Darrell, “Adversarial feature learning,” *arXiv preprint arXiv:1605.09782*, 2016.
- [15] P. Mildenerger, M. Eichelberg, and E. Martin, “Introduction to the dicom standard,” *European radiology*, vol. 12, no. 4, pp. 920–927, 2002.
- [16] F. Eckstein, W. Wirth, and M. C. Nevitt, “Recent advances in osteoarthritis imaging—the osteoarthritis initiative,” *Nature Reviews Rheumatology*, vol. 8, no. 10, pp. 622–630, 2012.
- [17] J. Deng, W. Dong, R. Socher, L.-J. Li, K. Li, and L. Fei-Fei, “Imagenet: A large-scale hierarchical image database,” in *2009 IEEE conference on computer vision and pattern recognition*, pp. 248–255, Ieee, 2009.
- [18] R. Zhang, P. Isola, and A. A. Efros, “Colorful image colorization,” in *European conference on computer vision*, pp. 649–666, Springer, 2016.
- [19] J. Donahue and K. Simonyan, “Large scale adversarial representation learning,” *arXiv preprint arXiv:1907.02544*, 2019.
- [20] E. Pierson, D. M. Cutler, J. Leskovec, S. Mullainathan, and Z. Obermeyer, “An algorithmic approach to reducing unexplained pain disparities in underserved populations,” *Nature Medicine*, vol. 27, no. 1, pp. 136–140, 2021.
- [21] Y. Lei, J. Harms, T. Wang, Y. Liu, H.-K. Shu, A. B. Jani, W. J. Curran, H. Mao, T. Liu, and X. Yang, “Mri-only based synthetic ct generation using dense cycle consistent generative adversarial networks,” *Medical physics*, vol. 46, no. 8, pp. 3565–3581, 2019.
- [22] D. Hsu and G. A. Marshall, “Primary and secondary prevention trials in alzheimer disease: looking back, moving forward,” *Current Alzheimer Research*, vol. 14, no. 4, pp. 426–440, 2017.
- [23] L. L. Raket, “Statistical disease progression modeling in alzheimer disease,” *Frontiers in big Data*, vol. 3, 2020.
- [24] M. Louis, R. Couronné, I. Koval, B. Charlier, and S. Durrleman, “Riemannian geometry learning for disease progression modelling,” in *International Conference on Information Processing in Medical Imaging*, pp. 542–553, Springer, 2019.
- [25] G. Lee, K. Nho, B. Kang, K.-A. Sohn, and D. Kim, “Predicting alzheimer’s disease progression using multi-modal deep learning approach,” *Scientific reports*, vol. 9, no. 1, pp. 1–12, 2019.
- [26] L. Pimpin, H. Cortez-Pinto, F. Negro, E. Corbould, J. V. Lazarus, L. Webber, N. Sheron, E. H. S. Committee, *et al.*, “Burden of liver disease in europe: epidemiology and analysis of risk factors to identify prevention policies,” *Journal of hepatology*, vol. 69, no. 3, pp. 718–735, 2018.
- [27] J. Compston, A. Cooper, C. Cooper, N. Gittoes, C. Gregson, N. Harvey, S. Hope, J. Kanis, E. McCloskey, K. E. Poole, *et al.*, “Uk clinical guideline for the prevention and treatment of osteoporosis,” *Archives of osteoporosis*, vol. 12, no. 1, p. 43, 2017.

- [28] B. Gorenek, A. Pelliccia, E. J. Benjamin, G. Boriani, H. J. Crijns, R. I. Fogel, I. C. Van Gelder, M. Halle, G. Kudaiberdieva, D. A. Lane, *et al.*, “European heart rhythm association (ehra)/european association of cardiovascular prevention and rehabilitation (eacpr) position paper on how to prevent atrial fibrillation endorsed by the heart rhythm society (hrs) and asia pacific heart rhythm society (aphrs),” *European journal of preventive cardiology*, vol. 24, no. 1, pp. 4–40, 2017.
- [29] A. Alkhatib, C. Tsang, A. Tiss, T. Bahorun, H. Arefanian, R. Barake, A. Khadir, and J. Tuomilehto, “Functional foods and lifestyle approaches for diabetes prevention and management,” *Nutrients*, vol. 9, no. 12, p. 1310, 2017.
- [30] S. M. McKinney, M. Sieniek, V. Godbole, J. Godwin, N. Antropova, H. Ashrafiyan, T. Back, M. Chesus, G. S. Corrado, A. Darzi, *et al.*, “International evaluation of an ai system for breast cancer screening,” *Nature*, vol. 577, no. 7788, pp. 89–94, 2020.
- [31] J. Petersen, P. F. Jäger, F. Isensee, S. A. Kohl, U. Neuberger, W. Wick, J. Debus, S. Heiland, M. Bendszus, P. Kickingereder, *et al.*, “Deep probabilistic modeling of glioma growth,” in *International Conference on Medical Image Computing and Computer-Assisted Intervention*, pp. 806–814, Springer, 2019.
- [32] J. Petersen, F. Isensee, G. Köhler, P. F. Jäger, D. Zimmerer, U. Neuberger, W. Wick, J. Debus, S. Heiland, M. Bendszus, *et al.*, “Continuous-time deep glioma growth models,” in *International Conference on Medical Image Computing and Computer-Assisted Intervention*, pp. 83–92, Springer, 2021.
- [33] A. Tiulpin, I. Melekhov, and S. Saarakkala, “Kneel: knee anatomical landmark localization using hour-glass networks,” in *Proceedings of the IEEE/CVF International Conference on Computer Vision Workshops*, pp. 0–0, 2019.
- [34] N. A. Segal, M. C. Nevitt, K. D. Gross, J. Hietpas, N. A. Glass, C. E. Lewis, and J. C. Torner, “The multicenter osteoarthritis study (most): opportunities for rehabilitation research,” *PM & R: the journal of injury, function, and rehabilitation*, vol. 5, no. 8, 2013.
- [35] M. Heusel, H. Ramsauer, T. Unterthiner, B. Nessler, and S. Hochreiter, “Gans trained by a two time-scale update rule converge to a local nash equilibrium,” in *Advances in Neural Information Processing Systems*, pp. 6626–6637, 2017.
- [36] M. S. Sajjadi, O. Bachem, M. Lucic, O. Bousquet, and S. Gelly, “Assessing generative models via precision and recall,” *arXiv preprint arXiv:1806.00035*, 2018.
- [37] D. P. Kingma and J. Ba, “Adam: A method for stochastic optimization,” *arXiv preprint arXiv:1412.6980*, 2014.
- [38] A. Paszke, S. Gross, F. Massa, A. Lerer, J. Bradbury, G. Chanan, T. Killeen, Z. Lin, N. Gimelshein, L. Antiga, *et al.*, “Pytorch: An imperative style, high-performance deep learning library,” *Advances in neural information processing systems*, vol. 32, pp. 8026–8037, 2019.
- [39] Z. C. Lipton and S. Tripathi, “Precise recovery of latent vectors from generative adversarial networks,” *arXiv preprint arXiv:1702.04782*, 2017.
- [40] A. Tiulpin, S. Klein, S. M. Bierma-Zeinstra, J. Thevenot, E. Rahtu, J. van Meurs, E. H. Oei, and S. Saarakkala, “Multimodal machine learning-based knee osteoarthritis progression prediction from plain radiographs and clinical data,” *Scientific reports*, vol. 9, no. 1, pp. 1–11, 2019.
- [41] J. Yim, R. Chopra, T. Spitz, J. Winkens, A. Obika, C. Kelly, H. Askham, M. Lukic, J. Huemer, K. Fasler, *et al.*, “Predicting conversion to wet age-related macular degeneration using deep learning,” *Nature Medicine*, vol. 26, no. 6, pp. 892–899, 2020.
- [42] D. Ardila, A. P. Kiraly, S. Bharadwaj, B. Choi, J. J. Reicher, L. Peng, D. Tse, M. Etemadi, W. Ye, G. Corrado, *et al.*, “End-to-end lung cancer screening with three-dimensional deep learning on low-dose chest computed tomography,” *Nature medicine*, vol. 25, no. 6, pp. 954–961, 2019.
- [43] T. Han, S. Nebelung, F. Pedersoli, M. Zimmermann, M. Schulze-Hagen, M. Ho, C. Haarbuerger, F. Kiessling, C. Kuhl, V. Schulz, *et al.*, “Advancing diagnostic performance and clinical usability of neural networks via adversarial training and dual batch normalization,” *Nature Communications*, vol. 12, no. 1, pp. 1–11, 2021.

- [44] H. C. Kniep, F. Madesta, T. Schneider, U. Hanning, M. H. Schönfeld, G. Schön, J. Fiehler, T. Gauer, R. Werner, and S. Gellissen, “Radiomics of brain mri: utility in prediction of metastatic tumor type,” *Radiology*, vol. 290, no. 2, pp. 479–487, 2019.
- [45] M. Englund, E. M. Roos, and L. Lohmander, “Impact of type of meniscal tear on radiographic and symptomatic knee osteoarthritis: a sixteen-year followup of meniscectomy with matched controls,” *Arthritis & Rheumatism: Official Journal of the American College of Rheumatology*, vol. 48, no. 8, pp. 2178–2187, 2003.

Supplementary information

Table S1: The knee radiograph datasets for the training, validation, and testing of the predictive model

	OAI dataset			MOST dataset
	Training & validation	Test	Total	External test
Number of unique patients	3,506	1,290	4,796	2,753
Number of radiographs	44,326	8,655	52,981	19,340
Number of patients without KLS labels	852	-	852	-
Number of radiographs without KLS labels	9,849	-	9,849	-
Male (%)	1,463 (41.7%)	529 (41.0%)	1,992 (41.5%)	1,206 (43.8%)
Age, mean (SD), years	60.6 (9.1)	60.3 (9.1)	60.7 (9.1)	62.5 (8.1)
Patient knees with KLS = 0	2,537	763	3,300	2,514
Patient knees with KLS = 1	1,528	395	1,923	1,350
Patient knees with KLS = 2	2,396	438	2,834	1,401
Patient knees with KLS = 3	1,013	192	1,205	1,731
Patient knees with KLS = 4	321	66	387	957
Knees with OA progression of $\Delta\text{KLS} > 1$	375	95	474	661

The semi-quantitative assessments, i.e., Kellgren & Lawrence scores (KLS) of fixed flexion knee radiographs were available for both OAI and MOST datasets. Abbreviations: SD, standard deviation; KLS, Kellgren & Lawrence scores.

Table S2: Performance metrics of individual radiologists in predicting OA onset and progression as a function of model assistance

Radiologist (Years of Experience)	Model prediction assistance	Sensitivity (%)	Specificity (%)	PPV (%)	NPV (%)	Cohen's Kappa
Radiologist 1 (8 years)	no	53.7	54.2	22.2	82.8	0.022
	yes	53.7	93.3	66.2	89.2	
Radiologist 2 (8 years)	no	30.5	80.3	27.4	82.6	0.068
	yes	49.5	95.4	72.3	88.6	
Radiologist 3 (7 years)	no	31.6	84.1	32.6	83.5	0.070
	yes	33.7	95.1	62.7	85.5	
Radiologist 4 (8 years)	no	22.1	89.8	34.4	82.6	0.127
	yes	47.4	92.1	59.2	87.8	
Radiologist 5 (4 years)	no	36.8	78.3	29.2	83.6	0.053
	yes	49.5	91.6	58.8	88.2	
Radiologist 6 (6 years)	no	54.7	58.1	24.1	84.1	0.223
	yes	70.5	66.2	33.7	90.2	
Radiologist 7 (17 years)	no	65.3	61.1	29.0	87.9	0.048
	yes	56.8	86.4	50.5	89.2	

Cohen's kappa was calculated as a measure of agreement between two tests from the same reader. Abbreviations: PPV: positive predictive value, NPV: negative predictive value.

Table S3: Diagnostic performance metrics of the unsupervised and supervised models in predicting OA onset and progression on the OAI test set. p-values relate to inter-model comparisons.

Prediction	ROC-AUC (95% CI)	p-value	Sensitivity (95% CI)	p-value	Specificity (95% CI)	p-value
OA progression						
our model	0.691 (0.621, 0.757)	-	0.579 (0.458, 0.696)	-	0.743 (0.715, 0.772)	-
supervised model	0.524 (0.451, 0.597)	<0.001	0.611 (0.492, 0.727)	0.668	0.448 (0.416, 0.479)	0.011

P-values relate to a pairwise comparison between our model and the supervised model

Table S4: Diagnostic performance metrics of the unsupervised and supervised models in predicting OA onset and progression on the MOST test set. p-values relate to inter-model comparisons.

Prediction	ROC-AUC (95% CI)	p-value	Sensitivity (95% CI)	p-value	Specificity (95% CI)	p-value
OA progression						
our model	0.643 (0.596, 0.689)	-	0.614 (0.529, 0.699)	-	0.572 (0.539, 0.605)	-
supervised model	0.536 (0.481, 0.589)	<0.001	0.430 (0.341, 0.519)	0.001	0.618 (0.585, 0.650)	0.428

P-values relate to a pairwise comparison between our model and the supervised model

Table S5: Diagnostic performance metrics of the unsupervised model in predicting OA onset and progression on the OAI test set with variable amounts of training data.

Prediction	ROC-AUC (95% CI)	p-value	Sensitivity (95% CI)	p-value	Specificity (95% CI)	p-value
OA progression						
our system: 100% training data	0.691 (0.621, 0.757)	-	0.579 (0.458, 0.696)	-	0.743 (0.715, 0.772)	-
our system: 50% training data	0.668 (0.594, 0.738)	0.563	0.516 (0.393, 0.635)	0.497	0.782 (0.755, 0.808)	0.699
our system: 10% training data	0.578 (0.500, 0.656)	0.008	0.442 (0.323, 0.564)	0.188	0.715 (0.686, 0.744)	0.777
our system: 1% training data	0.538 (0.466, 0.607)	<0.001	0.547 (0.426, 0.667)	0.727	0.565 (0.533, 0.597)	0.070

P-values relate to a pairwise comparison between the model given full data and the models with partial data

Table S6: Diagnostic performance metrics of the unsupervised model in predicting OA onset and progression on the OAI test set with different numbers of nearest neighbors considered.

Prediction	ROC-AUC (95% CI)	p-value	Sensitivity (95% CI)	p-value	Specificity (95% CI)	p-value
OA progression						
our system: #nn=1	0.691 (0.621, 0.757)	-	0.579 (0.458, 0.696)	-	0.743 (0.715, 0.772)	-
our system: #nn=2	0.645 (0.572, 0.716)	0.290	0.588 (0.465, 0.704)	0.950	0.644 (0.614, 0.675)	0.318
our system: #nn=5	0.647 (0.577, 0.716)	0.328	0.601 (0.484, 0.718)	0.801	0.630 (0.599, 0.661)	0.267
our system: #nn=10	0.644 (0.575, 0.709)	0.295	0.631 (0.514, 0.745)	0.665	0.646 (0.615, 0.677)	0.341

P-values relate to a pairwise comparison between the model using one NN and the models using multiple NNs

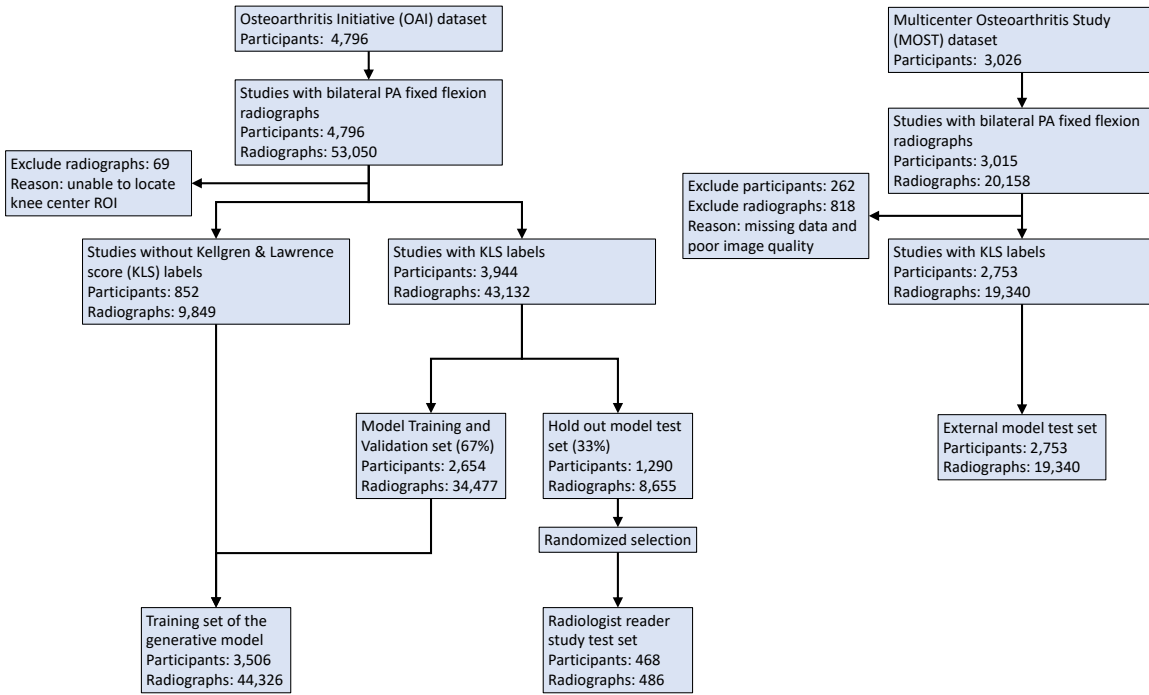


Fig. S1. Outline of the Data Processing Pipeline. The algorithm was trained on the multi-institutional OAI dataset which was subdivided into a training, validation, and testing set. The hold-out test set was isolated during development and exclusively used for testing. An additional test set was constructed by using the MOST dataset. After excluding knee radiographs with missing information or insufficient image quality, 19,340 radiographs remained on which the algorithm was additionally tested.

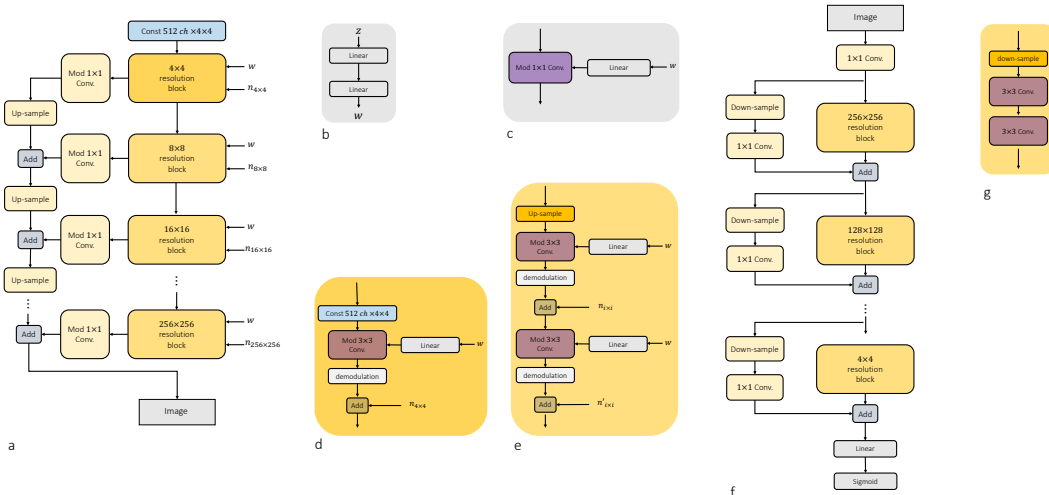


Fig. S2. Architectural Details of the Generative Model. (a) An architectural layout for the StyleGAN's G employed in our work. (b) A mapping network consists of 2 hidden linear layers followed by LReLU non-linear activations in G. (c) Details of the style modulated 1×1 convolution layer. The layer is used to convert feature maps to gray-scale radiographs. (d)-(e) Details about resolution blocks. The architecture of style-modulated 4×4 resolution block and higher blocks are shown in d and e, respectively. (f) An architectural layout for the used StyleGAN's D. To increase the performance of D, residual connections are added to fuse features of the previous resolution stage and the current ones. (g) Details of resolution blocks in D.

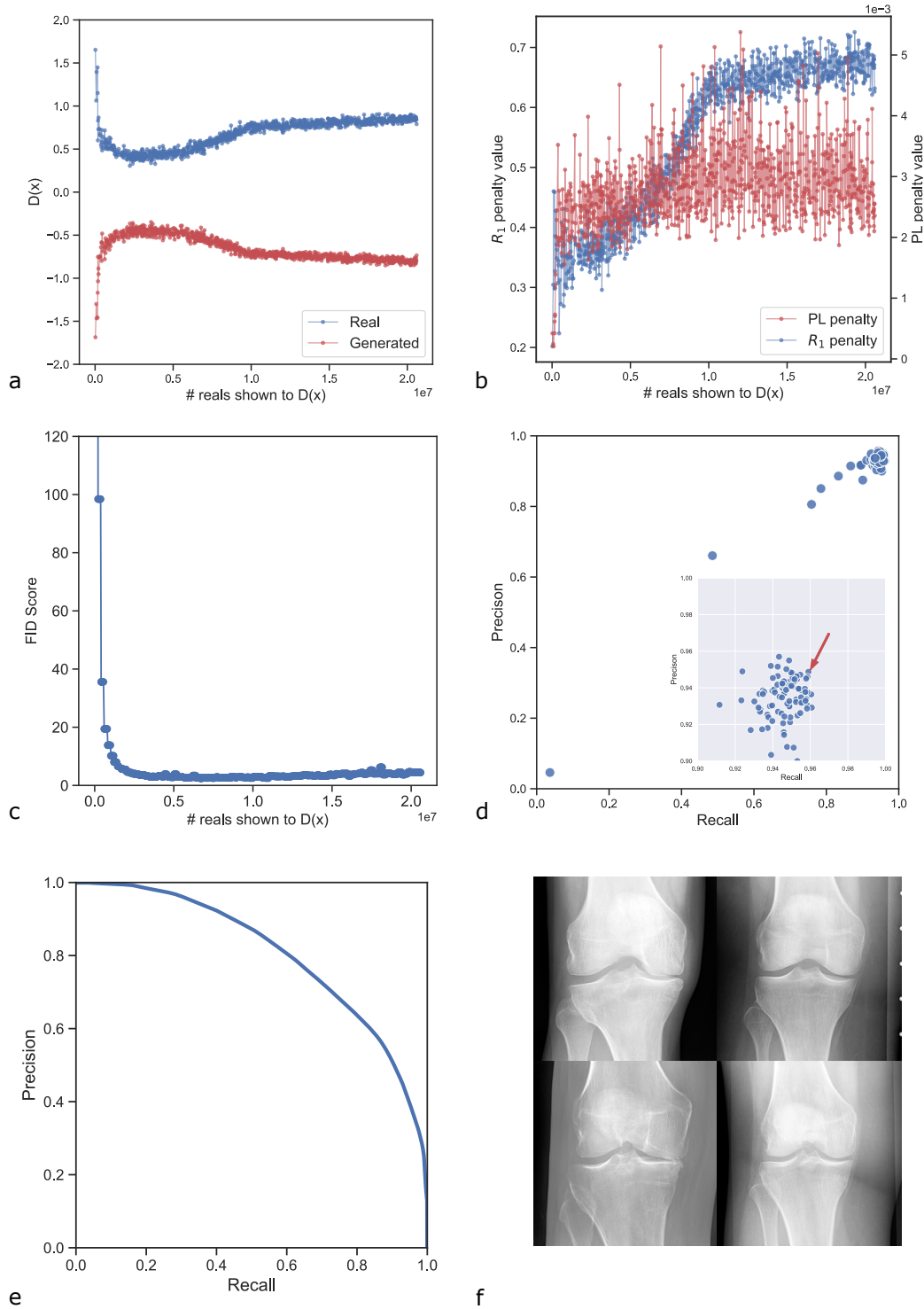


Fig. S3. Details of the Training Process and Performance Metrics of the Generative Adversarial Network (GAN). (a) Scores for real (blue) and synthetic radiographs along the training process of the GAN. Scores are stabilized after 10 million images. (b) Values of G (PL penalty) and D (R_1 penalty) penalties along the training process. (c) Fréchet Inception Distance (FID) scores along the training process to measure convergence to realistic radiographs. The convergence of the GAN is indicated by the FID scores plateauing after 10 million images are shown to the Discriminator. (d) Precision and recall metrics for different GAN models. The model with the highest precision and recall scores (as indicated by the red arrow) was selected. Inset tiled plot is a close-up of the right upper corner. (e) Further characterization of the best-performing GAN model via the corresponding distributional precision and recall curve [36]. (f) Examples of GAN-generated knee radiographs with a spatial resolution of 256×256 pixels.

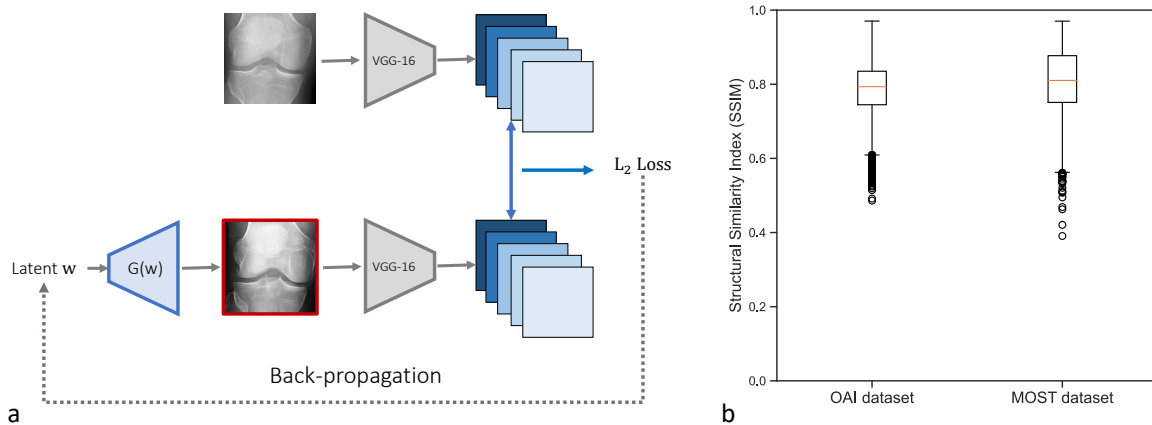


Fig. S4. Workflow Pipeline to Visualize the Embedding Procedure of a Representative Knee Radiograph into the Latent Space. (a) After computing the learned perceptual image patch similarity (LPIPS) loss, we freeze the parameters in G and the pretrained VGG net to exclusively optimize the intermediate latent w via back propagation. Representative original and synthetic radiographs are framed in gray and red, respectively. (b) In both OAI and MOST datasets, we characterize the embedding procedure by computing the Structural Similarity Index (SSIM) between original and synthetic radiographs. Lines and boxes indicate medians and upper or lower quartile, while whiskers detail the range of the data.

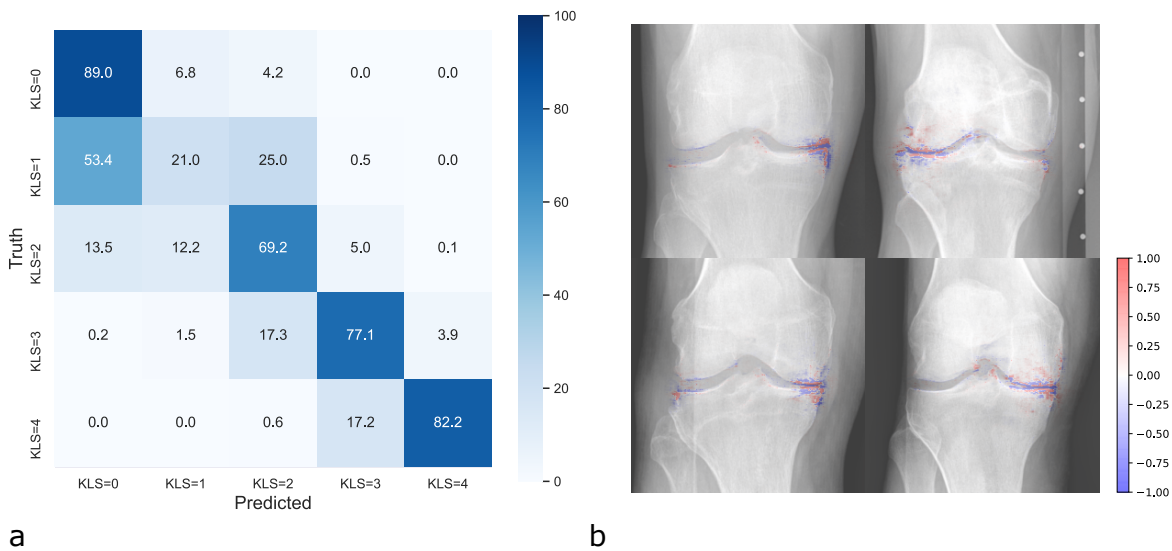


Fig. S5. Classification Performance of the Kellgren-Lawrence-Score (KLS) Classifier in the Progression Risk Estimation Module. (a) Confusion matrix of KLS of radiographic OA as predicted by the adversarially robust ResNet-50 model. (b) Loss gradients were plotted with respect to their input pixels for four radiographs of the OAI test set displaying signs of OA. Note that no extra pre-processing steps were applied to the loss gradients. Blue and red pixels denote negative and positive gradients and are centered around the joint space, indicating the plausibility and robustness of the classifier [43].

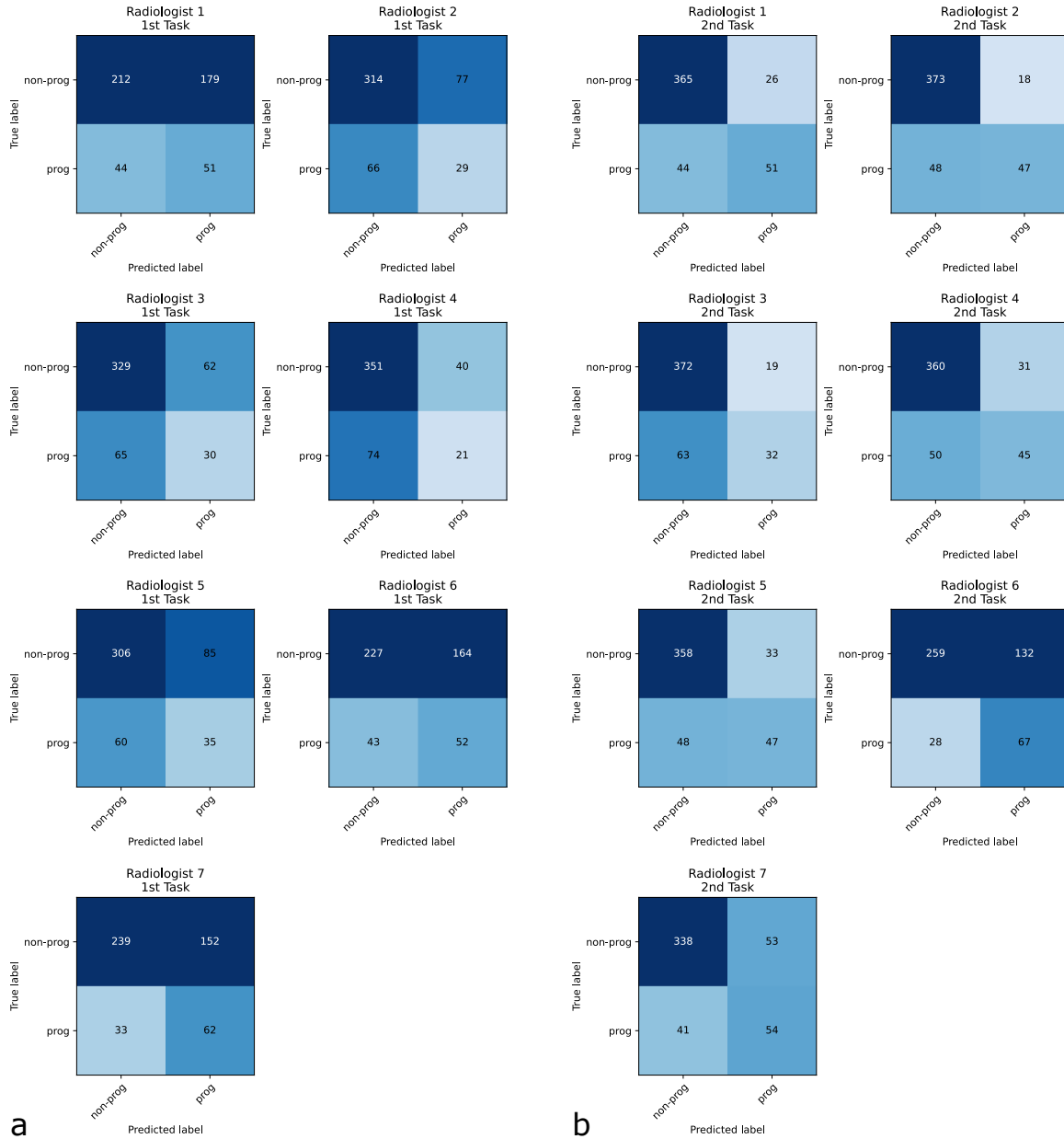


Fig. S6. Confusion Matrices for Each Radiologist and Experiment. Seven radiologists were tasked to judge whether a given knee radiograph is likely to undergo OA progression in the future (prog) or not (non-prog), based on the baseline radiograph alone (a) or on the baseline radiograph and the synthesized predicted radiograph (b). For both experiments, we randomly selected 486 knee radiographs from the OAI test set.

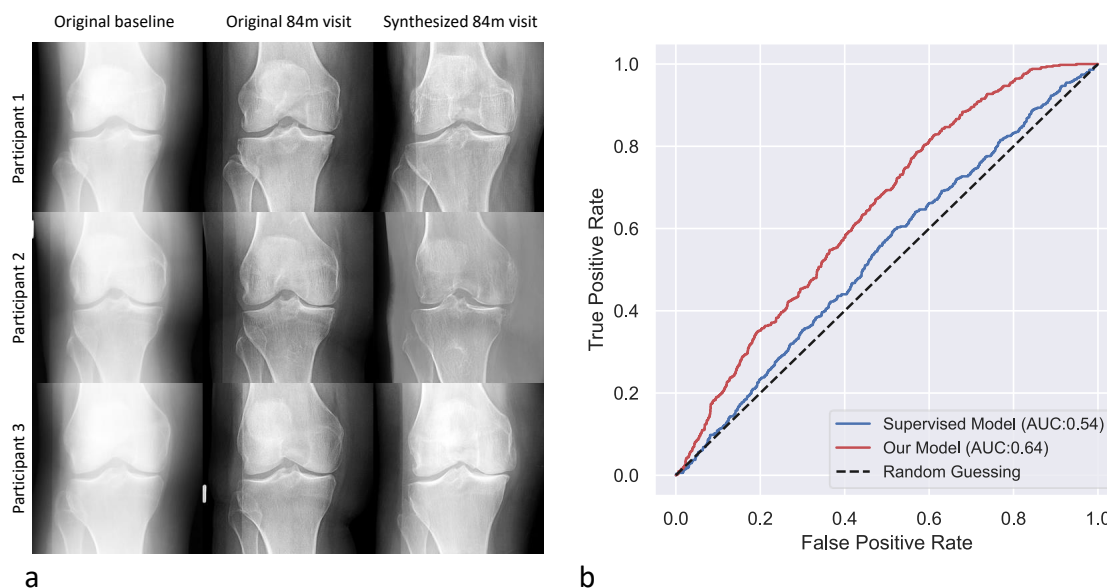


Fig. S7. Detailed Performance Metrics of the Predictive Model on the Multi-center Osteoarthritis Study (MOST) Dataset. Because the predictive model had been developed on data from the OAI, its predictive performance was additionally evaluated on unseen corresponding knee joint radiographs from the MOST dataset containing 2,753 participants and 19,340 radiographs. (a) Three representative participants with OA progression (listed row-wise). In the 3×3 grid, the 1st and 2nd columns present the original knee radiographs acquired at baseline and at the 84-month follow-up visit, while the 3rd column presents the predicted (synthetic) future radiograph. Even though some differences are present, the predicted radiographs demonstrate substantial correspondence with the original follow-up radiographs in terms of a clear OA signature. (b) ROC curves of the supervised classification network (blue) and unsupervised generative model (red) in determining OA progression at 84-month follow-up.

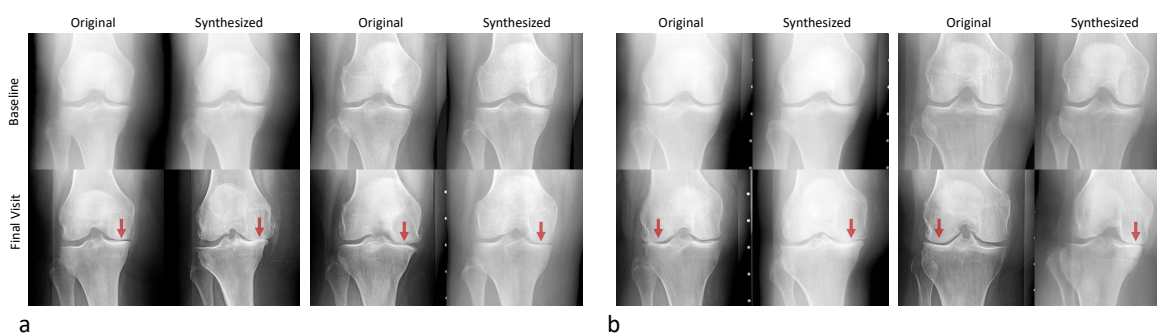


Fig. S8. Comparison of Correctly and Incorrectly Predicted Future Radiographs. Examples of Correctly (a) and Incorrectly (b) Predicted Radiographs. Original radiographs (left column of each 4×4 array) and synthesized radiographs (right column of each 4×4 array). While many synthesized radiographs correctly predicted the future course of OA (a), the predictive model failed in some instances and did not correctly predict progression altogether or predicted progression in the wrong compartment, e.g., medial instead of lateral (b). Joint space width narrowing is indicated by arrows. All examples were selected from the OAI test set.

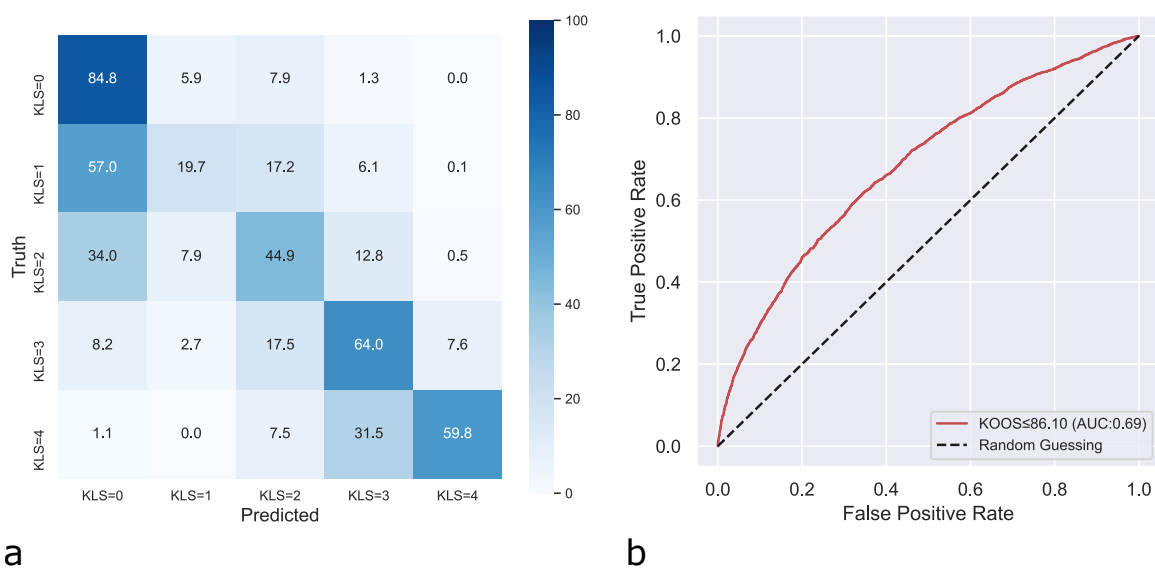


Fig. S9. Latent Features Contain Diagnostic Information. Exploring the information content of features learned by the predictive model (unsupervised StyleGAN), two classification tasks were performed solely on the low-dimensional latent code: KLS grading classification and severe knee pain classification. KLS was correctly predicted as demonstrated by the confusion matrix in (a). In addition, as shown in (b), we trained the shallow classifier on the task of heavy knee pain classification with a threshold of $KOOS \leq 86.1$ [45] and reached a state of the art ROC-AUC of 0.69 (95% CI: 0.651, 0.719) [20].